

# RSC Advances



This is an *Accepted Manuscript*, which has been through the Royal Society of Chemistry peer review process and has been accepted for publication.

*Accepted Manuscripts* are published online shortly after acceptance, before technical editing, formatting and proof reading. Using this free service, authors can make their results available to the community, in citable form, before we publish the edited article. This *Accepted Manuscript* will be replaced by the edited, formatted and paginated article as soon as this is available.

You can find more information about *Accepted Manuscripts* in the [Information for Authors](#).

Please note that technical editing may introduce minor changes to the text and/or graphics, which may alter content. The journal's standard [Terms & Conditions](#) and the [Ethical guidelines](#) still apply. In no event shall the Royal Society of Chemistry be held responsible for any errors or omissions in this *Accepted Manuscript* or any consequences arising from the use of any information it contains.



1 **Abstract**

2 Cu/Mg/Al/Zr hydrotalcite-like precursors with  $Zr^{4+}:(Al^{3+}+Zr^{4+})$  atomic ratios between  
3 0 and 1 were prepared by co-precipitation methods. The precursors were analyzed  
4 using X-ray diffraction (XRD), scanning electron microscope (SEM),  
5 thermogravimetric (TG) and Fourier Transform infrared spectroscopy (FT-IR). The  
6 results confirmed that well-defined layered double hydroxides (LDH) can be  
7 synthesized when the content of added Zr content is less than 0.25 in terms of  
8  $Zr^{4+}:(Al^{3+}+Zr^{4+})$  atomic ratio. The catalysts of Cu/Zn/Al/Zr mixed oxides can be  
9 obtained via thermal decomposition of hydroxides precursors, and can be used in  
10 dehydrogenation of 2-(1-cyclohexenyl) cyclohexanone (CHCH) to  
11 ortho-phenylphenol (OPP). Copper particles inside the catalyst act as active sites for  
12 dehydrogenation. Transmission electron microscope (TEM), XRD,  $N_2O$   
13 chemisorption and  $N_2$  adsorption-desorption were performed to investigate the effect  
14 of Zr content on determining the copper particle size. Based on the catalytic  
15 performance test, it was concluded that the conversion of CHCH depends on the  
16 copper particle size of these catalysts.

17 **Keywords:** Dehydrogenation; Cu/Mg/Al/Zr catalysts; Hydrotalcite;  
18 Ortho-phenylphenol

19

20

21

22

## 1 1. Introduction

2 Many investigations have been made on the dehydrogenation of alicyclic  
3 compounds. For instance, the only important industrial synthesis of o-phenylphenol  
4 (OPP) is still the cyclohexanone method, in which 2-(1-cyclohexenyl)cyclohexanone  
5 (CHCH) is obtained from cyclohexanone via aldol condensation and dehydration. At  
6 present, the catalysts used for OPP dehydrogenation generally use noble metals as the  
7 active ingredients such as Pt.<sup>1,2</sup> Only a few studies of the non-noble metals catalysts in  
8 the OPP synthesis process have been reported in literature.<sup>3</sup> Thus, the synthesis of  
9 non-precious metals dehydrogenation catalysts is very important to minimize both  
10 capital and operative expenses. Cu-based catalysts are applied in various industrial  
11 hydrogenation processes, and most of the catalysts when reduced with care can afford  
12 high dispersion of copper, showing good activity. However, the catalysts still suffered  
13 from thermal sintering and poisoning due to the poor dispersion. It is shown that the  
14 Cu-containing catalysts with high dispersion show good catalytic selectivity and  
15 activity in some reactions such as hydrogenation.<sup>4-6</sup> However, Cu-containing catalysts  
16 are not widely applied for dehydrogenation reactions of the organic compounds.

17 Hydrotalcite (HT)-like compounds are a new type of interesting materials which  
18 have been applied as ion exchangers, catalyst supports, catalysts, and composites.<sup>7-14</sup>  
19 Their empirical formula is  $[M^{II}_{1-x}M^{III}_x(OH)_2]^{x+}[A^{n-}_{x/n}]^{x-} \cdot mH_2O$ , where  $M^{II}$  is a  
20 divalent cation such as  $Cu^{2+}$ ,  $Zn^{2+}$ , or  $Mg^{2+}$ ,  $M^{III}$  is a trivalent cation such as  $Fe^{3+}$ ,  $Al^{3+}$ ,  
21 or  $Ga^{3+}$ .  $A^{n-}$  is an anion with a negative charge such as  $CO_3^{2-}$  and  $NO_3^-$ , and m is the  
22 molar amount of water in the interlayers.<sup>15,16</sup> The as-synthesized metallic oxides

1 exhibit highly homogeneously dispersed  $M^{3+}$  and  $M^{2+}$  at the atomic level, high  
2 specific surface area, high sintering stability, and strongly basic properties.<sup>17-19</sup>  
3 Thermal treatments leads to dehydroxylation, dehydration, and destruction of  
4 interlayer anions, and form the basic metallic oxides with high surface area, high  
5 dispersion of the active centers and better resistance to sintering.<sup>20</sup> The homogeneous  
6 distributions of metallic oxides in precursors can form the highly dispersed and much  
7 stable active metallic centers on catalyst surface after calcination and reduction.<sup>21</sup>  
8 Thus, well dispersed Cu-based catalysts with high stability, large surface area, and  
9 moderate or strong basic properties can be synthesized via the thermal decomposition  
10 of the hydrotalcite-like precursors.

11 In addition, the dispersibility and size of copper particles might significantly affect  
12 the stability of the catalyst. Some literatures reported the relevant deactivation  
13 mechanism for commercial catalysts.<sup>22-24</sup> The low catalytic stability is currently a  
14 limiting factor in applying Cu-containing catalysts in the hydrogenation process. How  
15 to solve this problem is still the key to applying the Cu-containing catalysts in the  
16 hydrogenation process. The introduction of Zr has been reported to improve the  
17 surface basicity and Cu dispersion, and hence to influence the activity of catalysts.<sup>25-28</sup>  
18 Furthermore, the presence of Zr can provide high stability and resistance to redox  
19 cycles.<sup>29</sup> However, very few studies reported the effect of addition of zirconium on  
20 tuning the particle size of Cu inside the catalyst. The detailed structure–activity  
21 relationship of the Zr-Cu material is hence lacking and is the subject of this work.

22 In this work, a series of Cu/Mg/Al/Zr catalysts obtained from Cu/Mg/Al/Zr layered

1 double hydroxides were prepared with  $Zr^{4+}/(Al^{3+}+Zr^{4+})$  atomic ratios between 0 and 1.  
2 Catalyst were characterized using X-ray diffraction (XRD), scanning electron  
3 microscope (SEM),  $N_2$  adsorption-desorption, transmission electron microscope  
4 (TEM), high-magnification transmission electron microscope (HRTEM),  $N_2O$   
5 chemisorption, thermogravimetric (TG),  $H_2$  temperature programmed reduction  
6 ( $H_2$ -TPR), Fourier transform infrared spectroscopy (FT-IR) and  $CO_2$  temperature  
7 programmed desorption ( $CO_2$ -TPD).

## 8 9 **2. Experimental**

### 10 **2.1. Preparation of Catalysts**

11 The Cu/Mg/Al/Zr hydrotalcite-like samples were prepared by co-precipitation  
12 method. The  $Cu^{2+}/Mg^{2+}/(Al^{3+}+Zr^{4+})$  atomic ratio was kept at 2.5:3.5:2 in the starting  
13 solution, while the atomic ratio of  $Zr^{4+}/Al^{3+}$  was changed from 0 to 1. Calculated  
14 amount of  $Cu(NO_3)_2 \cdot 3H_2O$ ,  $Mg(NO_3)_2 \cdot 6H_2O$ ,  $Zr(NO_3)_4 \cdot 5H_2O$  and  $Al(NO_3)_3 \cdot 9H_2O$   
15 were added into deionized water to prepare a 200mL mixed salt solution A, where the  
16 total concentration of  $(Cu^{2+}+Mg^{2+}+Al^{3+}+Zr^{4+})$  is 0.9 mol/L. Another solution (called  
17 B) was an aqueous of  $Na_2CO_3$  and NaOH, in which the concentration of  $Na_2CO_3$  and  
18 NaOH are both 1 mol/L. The A and B were slowly added to a four-necked flask with  
19 vigorous stirring and heated to the reaction temperature of 60 °C with the pH  
20 maintained at 9.5. The resulting precipitant were aged for 6 hour and recovered with  
21 filtration, then washed with distilled water to remove the trace sodium. Drying was  
22 performed in the air at 90 °C for 12 hours prior to the calcination conducted in air at

1 450 °C for 4 hours. Then the obtained powders were ground and extruded to strip  
2 catalysts. The catalysts were reduced using H<sub>2</sub> at 300 °C for 2 hours, followed by  
3 reacted at 330 °C. Synthesized Cu/Mg/Al/Zr catalysts were denoted as CMAZ-N,  
4 where N = 0, 1, 2, 3 and 4 denoting the Zr<sup>4+</sup>/(Al<sup>3+</sup>+Zr<sup>4+</sup>) ratio of 0, 0.25, 0.5, 0.75 and  
5 1, respectively.

## 6 7 **2.2. Characterization of Samples**

8 X-ray diffraction (XRD) patterns were measured by the X-ray diffraction  
9 instrument (Bruker AXS, D8 Advance) with the wavelength of the Cu K<sub>α</sub> radiation  
10 source being 1.5406Å. The intensity data was collected over the 2θ range of 5-70°  
11 with a step size of 0.05° and counting time of 1s each point under the condition of 40  
12 kV and 40 mA. SEM images of hydrotalcite-like precursors and catalysts were  
13 obtained by a field emission scanning electron microscopy (Hitachi, S-4800II).  
14 Thermal decomposition and stability for the catalyst precursors was studied by  
15 thermogravimetry analysis (TG-DTG, PerkinElmer Pyris 1) under the N<sub>2</sub> atmosphere  
16 (30 mL/min) with the heating rate of 10 °C /min from 50 °C to 750 °C. The infrared  
17 spectra of samples were recorded by a Fourier Transform spectroscopy (FT-IR, Bruker,  
18 Tensor 27), and measurements were performed in the wavenumber range of 400-4000  
19 cm<sup>-1</sup>. Transmission Electron Microscope (TEM) images of low-magnification were  
20 collected using a Tecnai 12 model machine for low-magnification observe samples.  
21 High-magnification Transmission Electron Microscope (HRTEM) was performed  
22 using Tecnai G2 F30 S-TWIN model machine for high-magnification to observe the

1 samples. The specific surface areas of the samples were computed from N<sub>2</sub>  
2 adsorption-desorption isotherms obtained at the temperature of liquid N<sub>2</sub> on a  
3 BELSORP-MAX instrument. Firstly, the powders were outgassed at the temperature  
4 of 200 °C for 6 h to ensure a clean surface before the measurement of the adsorption  
5 isotherms. H<sub>2</sub>-TPR was performed on the instrument Finesorb-3010. The catalyst was  
6 firstly treated in Ar (30 ml/min) with a 10 °C/min heating rate to 200 °C and kept it at  
7 200 °C for 30 min. After the samples were cooled down to 100 °C, TPR were  
8 conducted in the mixture of H<sub>2</sub>/Ar (molar ratio 1:9) flowing at 30 ml/min at a 10  
9 °C/min heating rate until 500 °C. Finally, the catalyst was cooled to room temperature  
10 in the presence of Ar. The exposed surface area of copper (S<sub>Cu</sub>) and the dispersion of  
11 copper (D<sub>Cu</sub>) were determined by adsorption of N<sub>2</sub>O and performed on Finesorb-3010  
12 instrument, using the method similar to that reported by Xia et al.<sup>30,31</sup> Catalysts were  
13 reduced (the procedure is described in TPR section) in H<sub>2</sub>/Ar (molar ratio 1:9)  
14 mixture with a flow rate of 30 mL/min at a heating rate of 10 °C/min until 450 °C and  
15 was kept at 330 °C for 30 min. The consumption amount of H<sub>2</sub> in the TPR was  
16 recorded as *X*. Then the reactor bed was purged in Ar to 50 °C. The mixture of  
17 N<sub>2</sub>O/Ar (the molar ratio 1:4, 30 mL/min) was changed to oxidize copper atoms of  
18 surface to Cu<sub>2</sub>O at the temperature of 50 °C for 1 hour. The reactor bed was then  
19 flushed with pure Ar to get rid of the oxidant. Another TPR procedure was conducted  
20 in the mixture of H<sub>2</sub>/Ar (molar ratio 1:9) with a flow rate of 30 mL/min at a 10 °C/min  
21 heating rate up to 330 °C and was kept at 330 °C for 30 min. The consumption of H<sub>2</sub>  
22 in this TPR procedure was recorded as *Y*. The exposed surface area of copper and the

1 dispersion of copper were computed by the following equations:

$$2 \quad S_{Cu} = (2Y \times N_A) / (1.4 \times 10^{19} \times X \times M_{Cu}) (m^2 \cdot g^{-1}) \quad (1)$$

$$3 \quad D_{Cu} = \frac{2Y}{X} \times 100\% \quad (2)$$

4 where  $S_{Cu}$  is the exposed surface area of Cu per gram sample,  $D_{Cu}$  is the dispersion of  
5 Cu,  $M_{Cu}$  the Cu atomic mass,  $N_A$  is Avogadro constant, and  $1.4 \times 10^{19}$  is the number of  
6 Cu atoms per  $m^2$ .<sup>32</sup> The basicity of catalysts was measured by CO<sub>2</sub> temperature  
7 programmed desorption (CO<sub>2</sub>-TPD, Finesorb-3010). The catalysts were firstly treated  
8 with Ar (30 ml/min) by raising the temperature at the rate of 10 °C/min to 330 °C and  
9 keep it for 30 min. Catalysts were saturated with carbon dioxide (30 ml/min) for 60  
10 min after cooling to 100 °C, and then flushed in Ar (30 ml/min) to get rid of all  
11 physical adsorbed molecules for 30 min. Finally, the TPD were performed in Ar (30  
12 ml/min) flowing at a 10 °C/min heating rate until 600 °C. Finally, the catalyst was  
13 cooled to room temperature in the presence of Ar.

### 15 2.3 Catalytic Reactions

16 The dehydrogenation reactions of CHCH were performed in a home-made set-up  
17 with a tubular quartz glass flow reactor ( $\Phi 19 \times 560$  mm). The reactor temperature was  
18 measured by a thermocouple located in the middle of the catalyst bed. The  
19 dehydrogenation reactions were carried out at 330 °C and atmospheric pressure. All  
20 catalysts were pre-treated by reduction under H<sub>2</sub> (flow rate of 20 mL/min) at 300 °C  
21 for 2 hours. Adjusting the H<sub>2</sub> flow rate at 10 mL/min, the reagent was added into the  
22 reactor using a syringe pump. The reaction products were dissolved in alcohol and

1 cooled to room temperature and analyzed using a gas chromatograph equipped with a  
2 flame ionization detector (FID) detector.

### 3 **3. Results and Discussions**

#### 4 **3.1. Textural and Structural Properties of the Precursors**

5 The XRD patterns of the precursors are shown in Figure 1. It is shown that the  
6 structure crystallinity of the samples decreases with increase of Zr amount. The  
7 reflection peaks for CMAZ-0 and CMAZ-1 show a well-crystallized hydrotalcite  
8 structure (JCPDS 48-0601). The introduction of Zr in CMAZ-1 still exist the  
9 formation of hydrotalcite structure, which was also observed by Jeong and Gao et  
10 al.<sup>33,34</sup> But, further increasing the amount of Zr, the characteristic peaks of  
11 hydrotalcite structure disappeared and the amorphous structure occurred instead. The  
12 amorphous structure occurred probably because of the introduction of the distortions  
13 in the hydrotalcite sheets as a result of the replacement of Al<sup>3+</sup> by Zr<sup>4+</sup>.<sup>35</sup> Another  
14 reason may be the formation of amorphous precipitates (i.e. Mg and Zr salts of  
15 hydroxyl carbonates and hydroxides).<sup>36</sup> In these systems, hydrotalcite-like  
16 microcrystalline phases consisting of small poorly ordered layers are more likely to be  
17 present, leading to the loss of crystallinity for the samples. Therefore, we expect that  
18 Zr-containing hydrotalcite-like compounds are the main component in these  
19 precursors, especially for the composition of  $Zr^{4+}/(Al^{3+}+Zr^{4+})$  less than 0.25.

20 SEM images of all precursors are shown in Figure 2. It can be observed that a  
21 well-developed layered and plate-like structure of hydrotalcite prepared by  
22 co-precipitation method without Zr added, could be easily identified in Figure 2a.<sup>37,38</sup>

1 When the  $Zr^{4+}/(Al^{3+}+Zr^{4+})$  ratio is up to 0.25 (i.e. CMAZ-1), the materials still  
2 exhibits a plate-like structure of hydrotalcite, though a destructed morphology is  
3 observed (Figure 2b). Also, it can be found that the plate-like structures are  
4 dense-stacking and homogeneous. However, when the amount of Zr increases as  
5 shown in Figures 2c-e, platelet particles tend to break into small pieces for another  
6 three samples<sup>35</sup> These samples consist of irregular particles that existed in diverse and  
7 larger agglomerates with poor crystallinity, which is consistent with the XRD results.  
8 We can conclude that the Zr/Al ratio has an obvious influence on the crystal  
9 morphology.

10 FT-IR (Supporting Information) was used to identify anion-cation and bond types  
11 for the interlayers of the precursors, shown in Figure S1. The intense and broad band  
12 at about  $3500\text{ cm}^{-1}$  is ascribed to the bond stretching mode of  $H_2O$  molecules of  
13 interlayers and the hydroxyl groups on the layers ( $\nu_{OHstr}$ ). The broad bands show that  
14 the hydroxyl species are hydrogen bonded. A weak absorption band occurs at about  
15  $1600\text{ cm}^{-1}$  because of the deformation bending modes of  $H_2O$  molecules. The bands  
16 between  $1300$  and  $1550\text{ cm}^{-1}$  are due to bonding stretching modes of the carbonate  
17 species. CMAZ-0 and CMAZ-1 exhibit medium vibration at about  $420\text{ cm}^{-1}$  ascribed  
18 to O-Metal-O bonds in the sheets. This vibration band gradually disappeared, which  
19 can be ascribed to the increase of the Zr content.<sup>36</sup> It also shows that introduction of  
20 Zr has a significant effect on the crystallinity of hydrotalcite layer structure.

21 To clarify the thermal decomposition process during the calcination, TG and  
22 differential thermal gravity (DTG) analysis techniques were performed (Figure S2 in

1 the Supporting Information). The results show that there are three major weight losses  
2 for all samples. The first peak of weight loss occurred at 100-200 °C, which can be  
3 ascribed to the removal of physically adsorbed H<sub>2</sub>O molecules in the interlayers. This  
4 suggests that the temperature around 150 °C was sufficient for the removal of  
5 physisorbed water. The second weight loss occurred at 250-400 °C, which may be  
6 ascribed to the decomposition of carbonate ions and laminates hydroxy dehydration.  
7 There are some differences for the third weight loss in these materials. The peak of  
8 weight loss peak for CMAZ-0 occurred at 600-650 °C. The weight loss peak for  
9 CMAZ-1 drops to 500-550 °C compared to CMAZ-0, which is ascribed to the  
10 introduction of Zr in the structure. This might reduce the electrostatic interaction  
11 between the anions and layers, that can result in lower thermal stability.<sup>39,40</sup> For the  
12 three samples of CMAZ-2, -3 and -4, the third stage almost disappeared, which  
13 implies that hydrotalcite laminate structure disappeared with the increase of Zr  
14 content.

### 15 **3.2. Textural and Structural Properties of the Calcined Samples**

16 Figure 3 shows the XRD patterns for the samples calcined after H<sub>2</sub> reduction for 2  
17 hours. It can be seen that there are no characteristic peaks of hydrotalcite-like  
18 compounds in the XRD patterns. This shows the lamellar framework collapsed and  
19 the structure is decomposed. Therefore, crystalline compounds containing Mg and Al  
20 were not detected. There are no characteristic peaks of Zr in XRD patterns of  
21 CMAZ-0, CMAZ-1 and CMAZ-2, which indicate that Zr was also in the amorphous  
22 state.<sup>26,41</sup> Cu<sup>0</sup> is the main crystal phase in the CMAZ-0, CMAZ-1 and CMAZ-2. But,

1 with the increase of Zr content (CMAZ-3 and CMAZ-4), the monoclinic zirconia  
2 (m-ZrO<sub>2</sub>, 2θ = 31.5°) characteristic peak occurs.

3 To investigate the effect of Zr content on the size of copper particles, the  
4 full width at half maxima (FWHM) in the XRD patterns and the size of the copper  
5 particles for different samples are listed in Table 1. The FWHM of the Cu<sup>0</sup> particles  
6 was calculated by Gaussian equation and the  $d(\text{Cu}^0)_{\text{XRD}}$  was calculated by Scherrer  
7 formula (Equation 3).  
8

$$d(\text{Cu}^0) = \frac{K\lambda}{FWHM(\pi/180)\cos\theta} \quad (3)$$

9 Scherrer formula to calculate  $d(\text{Cu}^0)$  size of each catalyst (K=0.89; λ=0.154 nm).

10 The results show that the average size of Cu<sup>0</sup> crystalline was 3.97-13.23 nm after  
11 H<sub>2</sub> reduction. As the Zr content changes, the size of copper particles reaches the  
12 minimum value (3.97 nm) in these samples. Further increase of the Zr content results  
13 in the increase of the copper particles size. It is clear that the particle size of Cu is  
14 related to the amount of Zr added. Through adding the amount of Zr in the catalyst,  
15 the size of copper particles can be controlled. However, excessive introduction of Zr  
16 may cause the growth of copper particle.

17 Figure 4 shows a representative set of TEM images for copper particles synthesized  
18 at two different compositions (CMAZ-1 and CMAZ-2) with the statistics of size  
19 distributions for copper particles in Figure 4. The mean diameter and min/max  
20 diameter were calculated by counting 100 particles (CMAZ-1) and 50 particles  
21 (CMAZ-2) with a loupe from the TEM image of 195000 magnifications. From Figure  
22 3 we can observe that CMAZ-1 and CMAZ-2 only present characteristic peaks of

1 copper. Thus, we can confirm that particles in these two samples are copper  
2 nanoparticles, which is confirmed by Zhang et al.<sup>42</sup> A copper particle size on surface  
3 of CMAZ-1 and CMAZ-2 was obtained from the corresponding size histograms. For  
4 CMAZ-1, the average particle size is 3.85 nm, which is smaller than 7.79 nm for  
5 CMAZ-2. It can be observed that copper particles are well dispersed in the oxide  
6 matrix. Additionally, the dispersion of copper particles in CMAZ-1 is much better  
7 than that CMAZ-2. This means that the introduction of Zr can tune the size of the  
8 copper particles and have a significant impact on the dispersion of the copper particles  
9 in the catalyst.<sup>29</sup> In order to fully understand the inner structure of Cu particles in  
10 CMAZ-1, the high-magnification TEM (HRTEM) are obtained shown in Figure 5. Cu  
11 particles size in Figure 5(a) is corresponding to the CMAZ-1 sample. Figure 5(b)  
12 depicts the fringe spacing of 0.21nm ensures the presence of Cu (111) plane. HRTEM  
13 elemental mapping images is shown in Figure S3 (Supporting Information), each  
14 element is well dispersed in the catalyst, which illustrated the high dispersion of  
15 Cu/Mg/Al/Zr catalyst.

16 The pore volume and surface area of the catalysts after reduction are shown in  
17 Table 2. The adsorption and desorption isotherms of samples are shown in Figure S4  
18 (Supporting Information).The maximum surface area is 134.07 m<sup>2</sup>·g<sup>-1</sup> possessed by  
19 CMAZ-1. Although CMAZ-0 surface area compare with CMAZ-1 is almost the same  
20 (133.11 m<sup>2</sup>·g<sup>-1</sup>), but the pore volume is nearly twice lower than CMAZ-1, respectively  
21 0.358 cm<sup>3</sup>·g<sup>-1</sup> and 0.789 cm<sup>3</sup>·g<sup>-1</sup>. It is speculated that the introduction of Zr may result  
22 in smaller particle size and larger surface area and pore volume. Conversely, surface

1 area and pore volume drop significantly in CMAZ-2, -3 and -4. This influence can be  
2 ascribed to distortion and destruction of hydrotalcite laminates. The distortion  
3 increases with the amount of Zr in the catalysts. The  $S_{\text{BET}}$  of catalysts decreases  
4 because of the destruction and distortion of hydrotalcite. The adsorption and  
5 desorption isotherms of samples are shown in Figure S4 (Supporting Information).

6 The exposed catalyst surface area and dispersion of Cu were measured by  $\text{N}_2\text{O}$   
7 adsorption and are shown in Table 2. When  $\text{Zr}^{4+}/(\text{Al}^{3+}+\text{Zr}^{4+})$  ratio is less than 0.25, the  
8 exposed surface area of Cu increased with the increase of Zr content. The addition  
9 of Zr also enhanced the Cu dispersion, which may be due to the effect of valence  
10 compensation and ion doping, i.e. the dissolved Zr in MgO crystal resulted in the  
11 formation of cation defects on the surface of Cu-MgO forming more active centers.<sup>43</sup>  
12 This is consistent with the results observed by Velu et al.,<sup>44,45</sup> who demonstrated that  
13 substitution of Zr could improve the dispersion of Cu. With further increase of the  
14 amount of Zr,  $\text{Zr}^{4+}$  may form the m- $\text{ZrO}_2$  crystalline structure and cause the decrease  
15 of the proportion of Zr placed in the layered structures.<sup>46</sup> Therefore, the existence of  
16 m- $\text{ZrO}_2$  with little  $\text{Zr}^{4+}$  in the layered structures caused the lower  $D_{\text{Cu}}$  for the CMAZ-2,  
17 CMAZ-3 and CMAZ-4.

18 FT-IR spectra of calcined samples are shown in Figure S5 (Supporting Information).  
19 Compared with the spectra of the precursors, the stretching vibration and absorption  
20 bands positions were retained meaning that the layered structure of hydrotalcite is not  
21 completely destroyed at the calcination temperature of 450 °C.

22 Figure 6 shows the  $\text{H}_2$ -TPR profiles for the calcined samples. As shown in Figure 6,

1 the TPR profiles for all samples with various amount of Zr show a broad band of H<sub>2</sub>  
2 consumption at the range of 150-400 °C. To get more insights into TPR results, the  
3 band of H<sub>2</sub> consumption were deconvoluted into two Gaussian forms denoted as  $\alpha$  and  
4  $\beta$  peaks, respectively. The peak positions and corresponding contributions are listed in  
5 the Table 3. The two peaks are attributed to the reduction of two different types of  
6 CuO phase. The  $\beta$  peak at high temperature is due to the reduction of dispersed CuO.  
7 The  $\alpha$  peak is attributed to the reduction of highly dispersed CuO appearing at low  
8 temperature.<sup>47</sup> As shown in Table 3,  $\alpha$  peak proportion in CMAZ-0 only is 14.97 %,   
9 the lowest Cu content of all the samples. The proportion suddenly increased to  
10 85.32 % in CMAZ-1 and reached the maximum. With the increasing amount of the Zr,  
11 this proportion decreases. The addition of Zr caused the broad  $\alpha$  peak for the highly  
12 dispersed CuO phase. It is because Zr can strengthen the interactions of the Cu<sup>+</sup>/Cu<sup>2+</sup>,  
13 leading to the higher reduction temperature.<sup>35</sup> Excessive Zr amount assists to form the  
14 m-ZrO<sub>2</sub>, as observed in the XRD profile (Figure 3), thus resulting in the decrease of  $\alpha$   
15 peak proportion.

16 The surface basicity of the catalysts was detected with CO<sub>2</sub>-TPD and is shown in  
17 Figure 7. The broad band of CO<sub>2</sub> consumption was deconvoluted into three Gaussian  
18 forms denoted as weakly ( $\alpha$  peak), moderately ( $\beta$  peak) and strongly ( $\gamma$  peak) basic  
19 sites. The weakly basic sites are ascribed to hydroxyl groups, moderately basic sites  
20 were related to Al-O, Zr-O or Mg-O pairs, and strongly basic sites can be related to  
21 oxygen atoms with low coordinations.<sup>35,47</sup> The peak positions and corresponding  
22 contributions are also shown in Table 4. The strength of strongly basic sites is

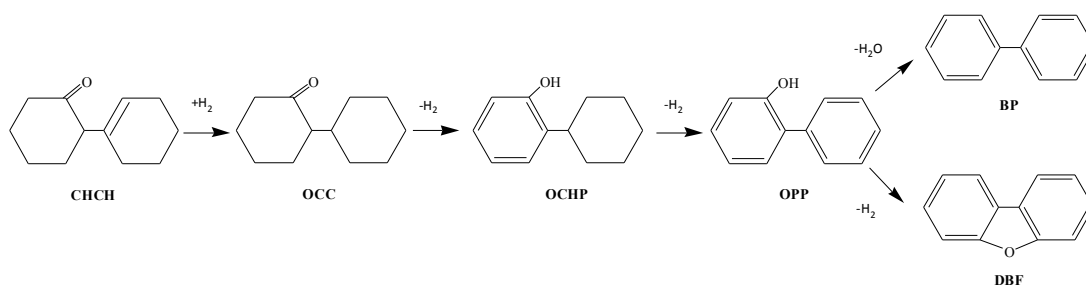
1 markedly enhanced for CMAZ-1 after the introduction of Zr. While, the strength of  
2 strongly basic sites decreased for subsequent CMAZ-2, CMAZ-3 and CMAZ-4. More  
3 specifically, in CMAZ-4, strongly basic sites disappeared. CMAZ-1 has the most  
4 strongly basic sites among these samples. The number of strongly basic sites increases  
5 because of the increase of Zr content in the layered structures. The higher electronic  
6 density of the layers in the samples with higher Zr content prohibits some oxygen  
7 atoms to coordinate with Zr atoms.<sup>48</sup> On the other hand, the number of strongly basic  
8 sites decreases with further increase of Zr amount in the catalysts due to the  
9 transformation of amorphous zirconia (am-ZrO<sub>2</sub>) to monoclinic zirconia (m-ZrO<sub>2</sub>)  
10 (observed in Figure 3). This transformation of structure may lead to less strongly  
11 basic sites.<sup>49</sup>

### 12 3.3. Catalytic Performance

14 Catalytic activity and selectivity of catalysts were tested in dehydrogenation of  
15 CHCH to OPP. Figure 8 shows the selectivity and conversions as a function of the  
16  $Zr^{4+}/(Zr^{4+}+Al^{3+})$  atomic ratio. Clear differences can be observed between the nature of  
17 the catalysts and corresponding catalytic performance. There is a significant change in  
18 the activity observed with the increase of the amount of Zr on these samples. The  
19 average conversion of CHCH reaches around 98 % for CMAZ-0 to CMAZ-3 and  
20 decreased to 67.5 % for CMAZ-4. The selectivity to OPP is also shown in Figure 8.  
21 There is a significant difference for these samples. The selectivity of OPP reached a  
22 maximum for  $Zr^{4+}/(Zr^{4+}+Al^{3+})$  atomic ratio 0.25 (CMAZ-1). Further increase in the

1 amount of Zr on the calcined samples leads to drastically toward 4.2 % with  
2  $Zr^{4+}/(Zr^{4+}+Al^{3+})$  atomic ratio of 1. Cu/Mg/Al/Zr catalysts with a better dispersion was  
3 prepared with the introduction of an appropriate Zr amount. In addition, the  
4 sintering of catalysts can be effectively inhibited because the catalysts can form with a  
5 more suitable structural morphology, which was an important factor. The enhanced  
6 crystallinity enables more surface area of the catalyst support of the active sites for  
7 dehydrogenation. The dehydrogenation performance follows the similar trend as that  
8 of dispersion of Cu. For CMAZ-1 where  $Zr^{4+}/(Zr^{4+}+Al^{3+})$  atomic ratio is low, the  
9 sample has a high pore volume as observed by BET measurement (Table 2). The  
10 catalysts exist in the form of the agglomeration of active sites at high  $Zr^{4+}/(Zr^{4+}+Al^{3+})$   
11 atomic ratio resulting in large-sized particles. From the  $CO_2$ -TPD profiles in Figure 7,  
12 the OPP selectivity is influenced by the distribution of basic sites on the surface of  
13 catalysts. The catalytic selectivity is also related to the amount of reducible copper,  
14 although the selectivity is not proportional to the atomic ratio of  $Zr^{4+}/(Zr^{4+}+Al^{3+})$   
15 shown in Figure 8. The appropriate amount of Zr added in the sample is 0.25 for the  
16 atomic ratio of  $Zr^{4+}/(Zr^{4+}+Al^{3+})$ .  $H_2$ -TPR results and reaction results confirmed this  
17 observation. CMAZ-1 shows the highest proportion of low temperature peak (around  
18 85.3 %) in  $H_2$ -TPR, and the better dispersed CuO in this sample. Guo and Wang et al.  
19 reported that catalytic activity of Cu-based dehydrogenation catalysts is related to  
20 well dispersed copper species.<sup>47, 50</sup> Therefore, the variation trends of catalytic activity  
21 of catalysts would be easy to understand in view of the similar trends of the dispersion  
22 of copper species, which was illustrated by XRD and TPR results. In addition, it is

1 clear that the OPP selectivity is also affected by the Zr amount, which tuned the  
2 dispersibility of copper species. The exposed surface area of copper measured by  
3 chemisorption of  $N_2O$  is an important parameter for Cu-containing catalysts. The  
4 catalytic activity depends on the exposed surface area of Cu. The exposed surface area  
5 of Cu increased obviously with the increase of Zr content. The maximum dispersion  
6 (22.5 %) of Cu is obtained for CMAZ-1 and the selectivity of OPP also reached a  
7 maximum. The number of strongly basic sites decreases with further increase of Zr  
8 amount in the catalysts because of the transformation of amorphous zirconia  
9 (am- $ZrO_2$ ) to monoclinic zirconia (m- $ZrO_2$ ). This structural transformation may lead  
10 to less strongly basic sites. Zhou et al. studied on Cu/ $ZrO_2$  catalysts, which consisted  
11 of tetragonal zirconia with Cu content lower than 10 wt%.<sup>51</sup> They referred to as the  
12 interaction between Cu species and the  $ZrO_2$  support which hindered the phase  
13 transformation to m- $ZrO_2$  based on the vacancy model of oxygen.<sup>52</sup>



14  
15 Scheme 1 Synthesis route of OPP from CHCH and its byproducts.

16 The goal of this investigation is to shed light on the effect of different Zr content on  
17 the catalytic properties in relation to byproducts. The dehydrogenation process  
18 consists of a sequence of hydrogenation or dehydrogenation reactions, in which the  
19 CHCH is successively transformed into o-cyclohexylcyclohexanone (OCC),

1 o-cyclohexylphenol (OCHP) and finally OPP (Scheme 1).<sup>53</sup> Besides, there are small  
2 amount of biphenyl (BP) and dibenzofuran (DBF) among byproducts. It is because  
3 that OPP can further dehydrogenated to DBF and dehydrated to BP. Catalytic  
4 selectivity for primary products of all catalysts is shown in Figure 9. When OPP  
5 selectivity increases, the byproducts OCC and OCHP naturally decrease. Moreover,  
6 OCC is the main byproducts. According to the route shown in the Scheme, the OPP  
7 selectivity is significantly affected by the amount of Zr. Mean Cu<sup>0</sup> crystalline sizes is  
8 the smallest in CMAZ-1 and OCC content is the lowest. This suggests that smaller  
9 copper particles size of catalyst results in the better copper dispersion. Thus, the  
10 conversion of CHCH to OPP is more effective. While mean Cu<sup>0</sup> crystalline sizes  
11 increases, copper distribution becomes worse. The conversion of CHCH mainly  
12 occurs in the first step reaction and the main byproduct is OCC. In conclusion, copper  
13 particle size has a significant effect on the OPP catalytic activity and selectivity. The  
14 introduction of Zr can control the copper particle size. The small mean Cu<sup>0</sup> crystalline  
15 size is in favor of the conversion of CHCH to OPP.

16 Figure 10 shows the catalytic selectivity to OPP with the reaction time. The  
17 corresponding conversions can be found in Table 1S (Supporting information). During  
18 the reactions, CMAZ-1 always shows the highest catalytic performance and the  
19 selectivity is still above 65% after 7 hours reaction. With the increase of Zr content,  
20 CMAZ-4 almost lost its catalytic activity. The copper particles size and high  
21 dispersion of containing active copper centers on surface have a significant impact on  
22 the catalytic stability. Chraska et al. studied the effect of the particle size on the

1 stability of the catalysts and observed that the stability for small particles can be  
2 illustrated by the lower surface energy of  $\text{ZrO}_2$ .<sup>54</sup> Purnama et al. observed a significant  
3 stabilizing effect of Cu centers in  $\text{ZrO}_2$ .<sup>55</sup> This may explain the stabilization of the Cu  
4 particles with a diameter of about 3 nm. It is clear that the CMAZ-1 catalyst prepared  
5 via co-precipitation method shows a stable catalytic performance during this reaction  
6 time.

#### 8 **4. Conclusion**

9 Cu-Mg-Al-Zr hydrotalcite-like compounds with different atomic ratio of  
10  $\text{Zr}^{4+}/(\text{Al}^{3+}+\text{Zr}^{4+})$  were successfully prepared by co-precipitation methods. The  
11 introduction of Zr can improve the catalytic properties of Cu-Mg-Al catalyst prepared  
12 via hydrotalcite-like precursors. The catalytic activity and selectivity for OPP  
13 synthesis are related to the size of Cu species and the amount of Zr in catalysts. The  
14 optimum content of Zr is about  $\text{Zr}^{4+}/(\text{Al}^{3+}+\text{Zr}^{4+}) = 0.25$  (CMAZ-1), showing the  
15 highest catalytic stability and selectivity above 65% even after 7 hours of reaction.  
16 The existence of Cu nanoparticles is confirmed by analysis using XRD, TEM and  
17 HRTEM. Introducing Zr affects the size of Cu nanoparticles, smaller Cu nanoparticles  
18 always shows the better catalytic performance ; and  $\text{CO}_2$ -TPD results show that Zr  
19 can lower the content of Al on the catalyst, and generate the strongly basic sites. This  
20 may weaken the interaction between  $\text{Al}_2\text{O}_3$  and CuO so to avoid the agglomeration of  
21 active sites. CMAZ-1 always shows the highest catalytic stability and the selectivity  
22 keep above 65% even after 7 hours reaction.

1

2 **Acknowledgements**

3 We thank Dr. Peyman Moghadam at Northwestern University and Prof. Gui Han at  
4 Yangzhou University for reading this manuscript and giving the valuable suggestions.

5 This work was supported by the Natural Science Foundation of China (Grant No.  
6 20806064 and 21106125), the Natural Science Foundation of Jiangsu Province, China  
7 (BK20131227). Generous allocations of test were provided by Testing Center of  
8 Yangzhou University and a Project funded by the Priority Academic Program  
9 Development of Jiangsu Higher Education Institutions.

10

11 **Supporting Information Available:** FT-IR, DG-DTG, N<sub>2</sub> adsorption-desorption  
12 isotherms and elemental mapping images of catalysts. This material is available free  
13 of charge via the Internet at <http://pubs.rsc.org>.

14

15

16

17

18

19

20

21

22

1  
References

- 2 1 H. Goto, N. Shibamoto, Process for preparing of o-phenylphenol, US  
3 patent 4088702, 1978.
- 4 2 I. Juichi, Process for the production of o-phenylphenol, US patent  
5 4080390, 1978
- 6 3 W. Oskar, H. Schwarz, Process for preparing hydroxypiphenyl, US patent  
7 3932536, 1976
- 8 4 K. V. R. Chary, G. V. Sagar, D. Naresh, K. K. Seela, B. Sridhar, *J. Phys.*  
9 *Chem. B*, 2005, **109**, 9437-9444.
- 10 5 J. Fei, Z. Hou, B. Zhu, H. Lou, X. Zheng, *Appl. Catal. A: General*, 2006,  
11 **304**, 49-54.
- 12 6 D. Jin, B. Zhu, Z. Hou, J. Fei, H. Lou, X. Zheng, *Fuel*, 2007, **86**,  
13 2707-2713.
- 14 7 J. L. Shumaker, C. Crofcheck, S. A. Tackett, E. Santillan-Jimenez, T.  
15 Morgan, Y. Ji, M. Crocker, T. J. Toops, *Appl. Catal. B: Environ*, 2008, **82**,  
16 120-130.
- 17 8 C. Xu, Y. Gao, X. Liu, R. Xin, Z. Wang, *RSC Adv.*, 2013, **3**, 793-801..
- 18 9 J. S. Valente, F. Tzompantzi, J. Prince, J. G. H. Cortez, R. Gomez, *Appl.*  
19 *Catal. B: Environ*, 2009, **90**, 330-338.
- 20 10 M. Jablonska, A. E. Palomares, L. Chmielarz, *Chem. Eng. J.*, 2013, **231**,  
21 273-280.
- 22 11 A. Hanif, S. Dasgupta, S. Divekar, A. Arya, M. O. Garg, A. Nanoti, *Chem.*

- 1           *Eng. J.*, 2014, **236**, 91-99.
- 2           12 J. Agrell, H. Birgersson, M. Boutonnet, *J. Power Sources* 2002, **106**,  
3           249-257.
- 4           13 Z. Yuan, Li. Wang, J. Wang, S. Xia, P. Chen, Z. Hou, X. Zheng, *Appl.*  
5           *Catal. B: Environ*, 2011, **101**, 431-440.
- 6           14 A. Serrano-Lotina, L. Rodriguez, G. Munoz, L. Daza, *J. Power Sources*,  
7           2011, **196**, 4404-4410.
- 8           15 F. Cavani, F. Trifiro, A. Vaccari, *Catal. Today*, 1991, **11**, 173-301.
- 9           16 Z. Jiang, Z. P. Hao, J. J. Yu, H. X. Hou, C. Hu, J. X. Su, *Catal. Today*,  
10           2005, **99**, 3-4.
- 11           17 A. Alejandro, F. Medina, P. Salagre, X. Correig, J. E. Sueiras, *Chem.*  
12           *Mater*, 1999, **11**, 939-948.
- 13           18 G. Busca, U. Costantino, F. Marmottini, T. Montanari, P. Patrono, F.  
14           Pinzari, G. Ramis, *Appl. Catal. A: General*, 2006, **310**, 70-78.
- 15           19 L. H. Zhang, C. Zheng, F. Li, D. G. Evans, X. Duan, *J. Mater. Sci.*, 2008,  
16           **43**, 237-243.
- 17           20 J. Barrault, A. Derouault, G. Courtois, J. M. Maissant, J. C. Dupin, C.  
18           Guimon, H. Martinez, E. Dumitriu, *Appl. Catal. A: General*, 2004, **262**,  
19           43-51.
- 20           21 A. F. Lucrédio, G. Jerkiewickz, E. M. Assaf, *Appl. Catal. A: General*,  
21           2007, **333**, 90-95.
- 22           22 D. Mott, J. Galkowski, L. Y. Wang, J. Luo, C. J. Zhong, *Langmuir*, 2007,

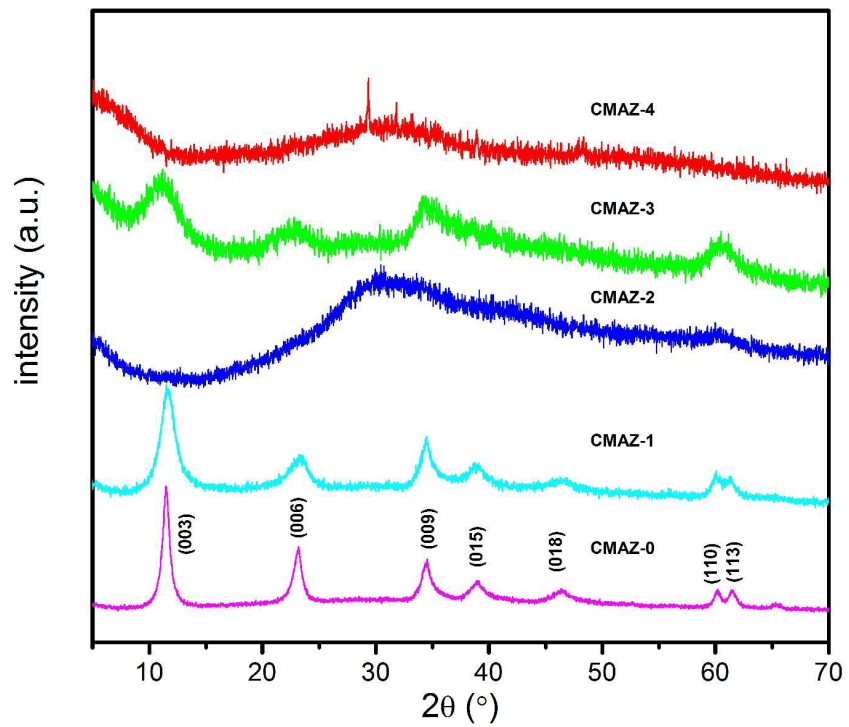
- 1           **23**, 5740-5745.
- 2           23 G. Prieto, J. Zecevic, H. Friedrich, K. P. de Jong, P. E. de Jongh, *Nature*
- 3           *Mater.*, 2013, **12**, 34-39.
- 4           24 C. T. Campbell, S. C. Parker, D. E. Starr, *Science*, 2002, **298**, 811-814.
- 5           25 A. Szizybalski, F. Girgsdies, A. Rabis, Y. Wang, M. Niederberger, T.
- 6           Ressler, *J. Catal.*, 2005, **233**, 297-307.
- 7           26 Y. F. Li, X. F. Dong, W. M. Lin, *Int. J. Hydrogen Energy*, 2004, **29**,
- 8           1617-1621.
- 9           27 J. H. Flores, D. P. B. Peixoto, L. G. Appel, R. R. de Avillez, M. I. P. da
- 10          Silva, *Catal. Today*, 2011, **172**, 218-225.
- 11          28 B. Lindstrom, L. J. Pettersson, *Int. J. Hydrogen Energy*, 2001, **26**,
- 12          923-933.
- 13          29 J. Agrell, H. Birgersson, M. Boutonnet, I. M. Cabrera, R. Navarro, J.
- 14          Fierro, *J. Catal.*, 2003, **219**, 389-403.
- 15          30 S. X. Xia, Z. L. Yuan, L. N. Wang, P. Chen, Z. Y. Hou, *Appl. Catal. A:*
- 16          *General*, 2011, **403**, 173-182.
- 17          31 S. X. Xia, R. F. Nie, X. Y. Lu, L. N. Wang, P. Chen, Z. Y. Hou, *J. Catal.*,
- 18          2012, **296**, 1-11.
- 19          32 S. X. Xia, L. P. Zheng, W. S. Ning, L. N. Wang, P. Chen, Z. Y. Hou, *J.*
- 20          *Mater. Chem. A*, 2013, **1**, 11548-11552.
- 21          33 H. Jeong, K. I. Kim, T. H. Kim, C. H. Ko, H. C. Park, I. K. Song, *J.*
- 22          *Power Sources*, 2006, **159**, 1296-1299.

- 1 34 G. Chen, N. Xu, X. Li, Q. Liu, H. Yang, W. Li, *RSC Adv.*, 2015, **5**,  
2 60128-60134.
- 3 35 P. Gao, F. Li, H. J. Zhan, N. Zhao, F. K Xiao, W. Wei, L. S. Zhong, H.  
4 Wang, Y. H. Sun, *J. Catal.*, 2013, **298**, 51-60.
- 5 36 S. Velu, D. P. Sabde, N. Shah, S. Sivasanker, *Chem. Mater.*, 1998, **10**,  
6 3451-3458.
- 7 37 D. G. Cantrell, L. J. Gillie, A. F. Lee, K. Wilson, *Appl. Catal. A: General*,  
8 2005, **287**, 183-190.
- 9 38 S. H. Wang, Y. B. Wang, Y. M. Dai, J. M. Jehng, *Appl. Catal. A: General*,  
10 2012, **439-440**, 135-141.
- 11 39 L. H. Zhang, F. Li, D. G. Evans, X. Duan, *Ind. Eng. Chem. Res.*, 2010, **49**,  
12 5959-5968.
- 13 40 X. X. Guo, F. Z. Zhang, D. G. Evans, X. Duan, *Chem. Commun.*, 2010,  
14 **46**, 5197-5210.
- 15 41 H. Oguchi, T. Nishiguchi, T. Matsumoto, H. Kanai, K. Utani, Y.  
16 Matsumura, S. Imamura, *Appl. Catal. A: General*, 2005, **281**, 69-73.
- 17 42 Q. Zhang, Y. Z. Zuo, M. H. Han, J. F. Wang, Y. Jin, F. Wei, *Catal. Today*,  
18 2010, **150**, 55-60.
- 19 43 X. An, J. L. Li, Y. Z. Zuo, Q. Zhang, D. Z. Wang, J. F. Wang, *Catal. Lett.*,  
20 2007, **118**, 264-269.
- 21 44 S. Velu, K. Suzuki, M. Okazaki, M. P. Kapoor, T. Osaki, F. Ohashi, *J.*  
22 *Catal*, 2000, **194**, 373-384.

- 1 45 S. Velu, K. Suzuki, M. P. Kapoor, F. Ohashi, T. Osaki, *Appl. Catal. A:*  
2 *General*, 2001, **213**, 47-63.
- 3 46 D. Tichit, N. Das, B. Coq, R. Durand, *Chem. Mater.*, 2002, **14**,  
4 1530-1538.
- 5 47 X. M. Guo, D. S. Mao, G. Z. Lu, S. Wang, G. S. Wu, *J. Catal.*, 2010, **271**,  
6 178-185.
- 7 48 Z. Y. Ma, C. Yang, W. Wei, W. H. Li, Y. H. Sun, *J. Mol. Catal. A: Chem.*,  
8 2005, **227**, 119-124.
- 9 49 Y. X. Liu, K. P. Sun, H. W. Ma, X. L. Xu, X. L. Wang, *Catal. Commun.*,  
10 2010, **11**, 880-883.
- 11 50 L. C. Wang, Q. Liu, M. Chen, Y. M. Liu, Y. Cao, H. Y. He, K. N. Fan, *J.*  
12 *Phys. Chem. C*, 2007, **111**, 16549-16557.
- 13 51 R. X. Zhou, T. M. Yu, X. Y. Jiang, F. Chen, X. M. Zheng, *Appl. Surf. Sci.*,  
14 1999, **148**, 263-270.
- 15 52 M. G. Sanchez, J. L. Gazquez, *J. Catal.*, 1987, **104**, 120-135.
- 16 53 Kimiaki Imafuku, Junko Oda, Kenshi Itoh, Hisashi Matsumura, *Bull.*  
17 *Chem. Soc. Japan*, 1974, 47, 1201-1202.
- 18 54 T. Chraska, A. H. King, C. C. Berndt, *Mater. Sci. Eng. A*, 2000, **286**,  
19 169-178.
- 20 55 H. Purnama, F. Girgsdies, T. Ressler, J. H. Schattka, R. A. Caruso, R.  
21 Schomäcker, R. Schlögl, *Catal. Lett.*, 2004, **94**, 61-68.
- 22

1  
2  
3  
4  
5  
6

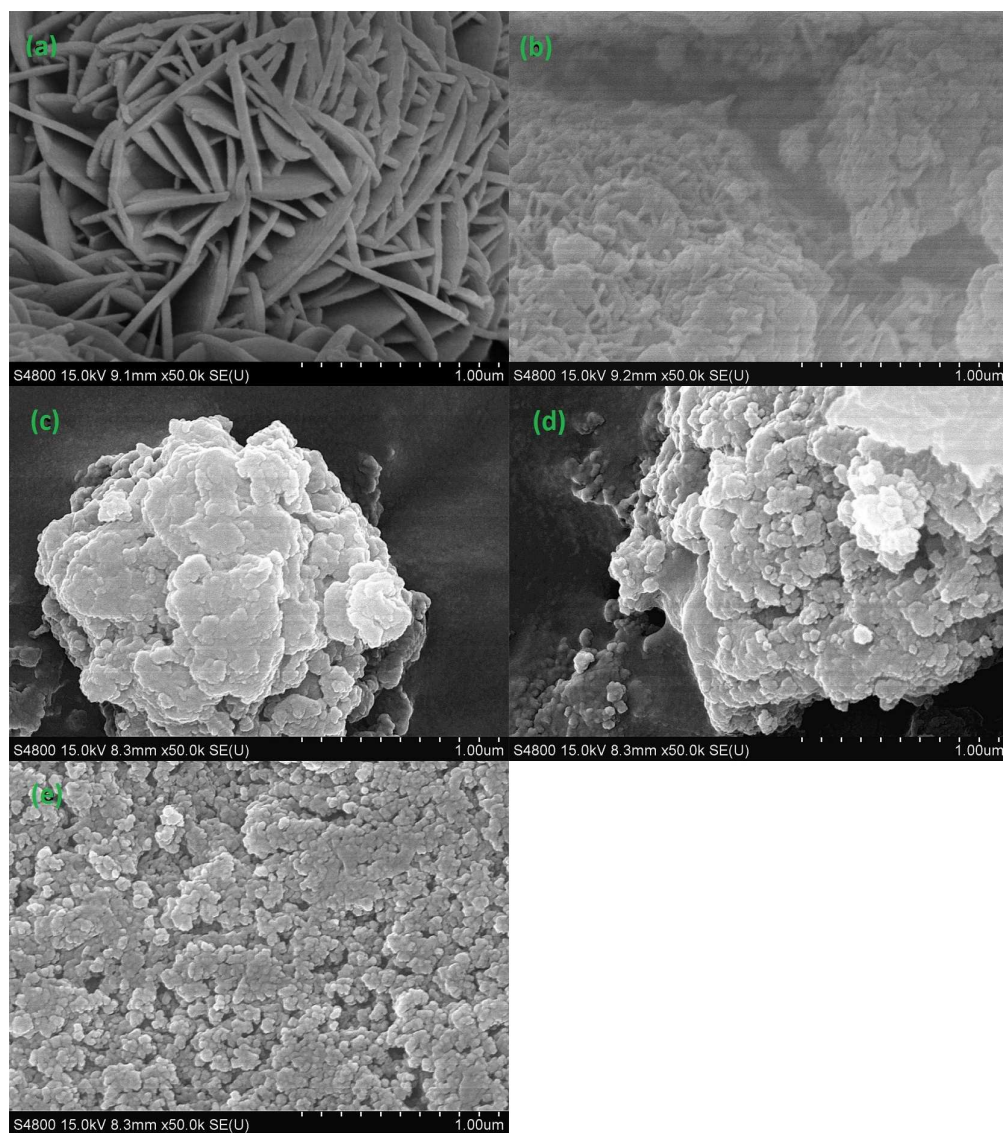
## Main Figures and Tables



7

**Fig. 1** XRD patterns of the Cu/Mg/Al/Zr precursors with various Zr content.

1



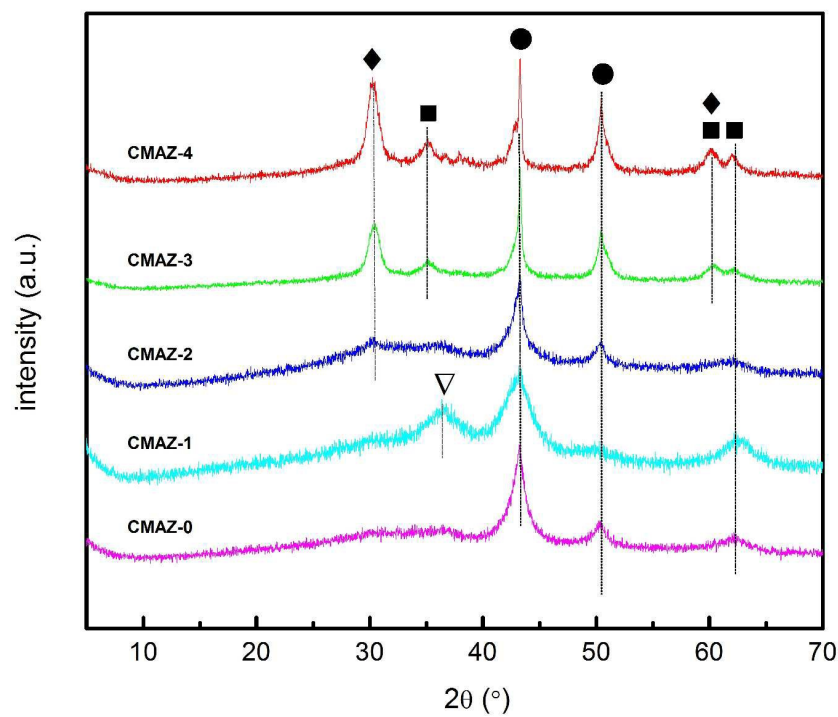
2

**Fig. 2** SEM images of uncalcined samples: (a) CMAZ-0, (b) CMAZ-1, (c) CMAZ-2,

3

(d) CMAZ-3, and (e) CMAZ-4.

1



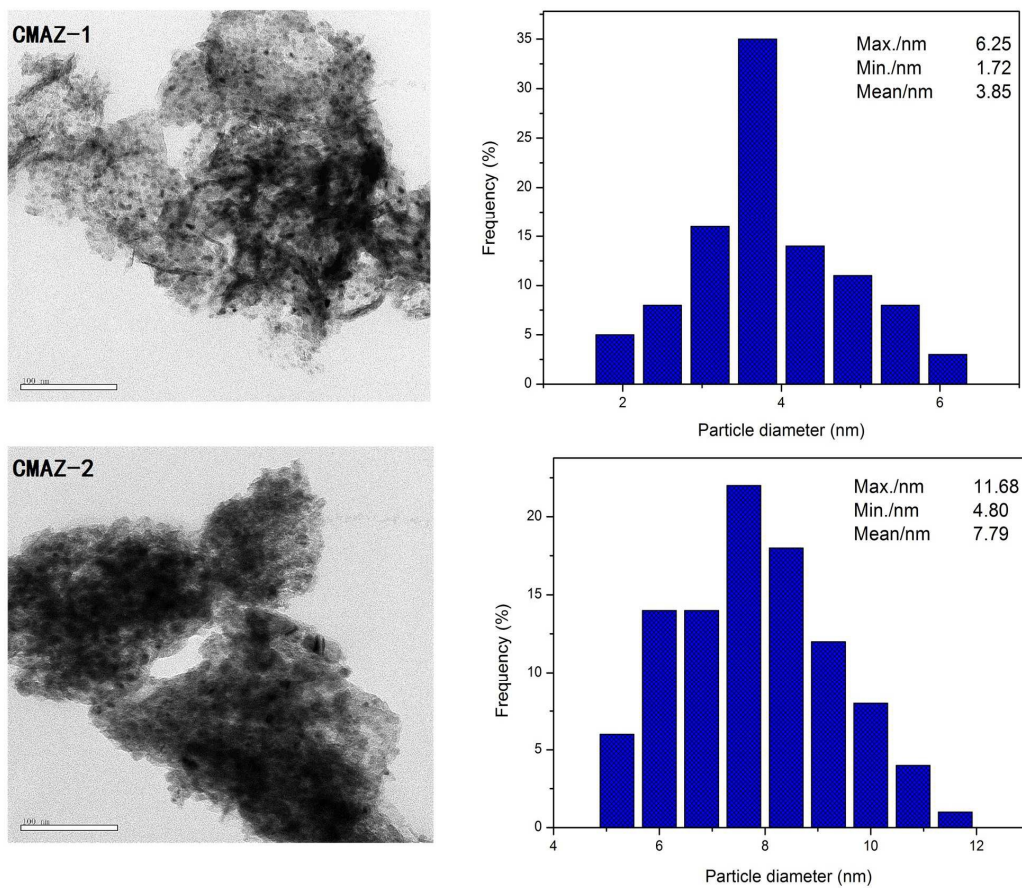
2

**Fig. 3** XRD patterns of the calcined Cu/Mg/Al/Zr catalysts after reduction at 300 °C.

3

(●) Cu<sup>0</sup>; (■) CuO; (▽) Cu<sub>2</sub>O; (◆) m-ZrO<sub>2</sub>

1



2

**Fig. 4** TEM images of CMAZ-1 and CMAZ-2 catalysts after H<sub>2</sub> reduction at 300 °C

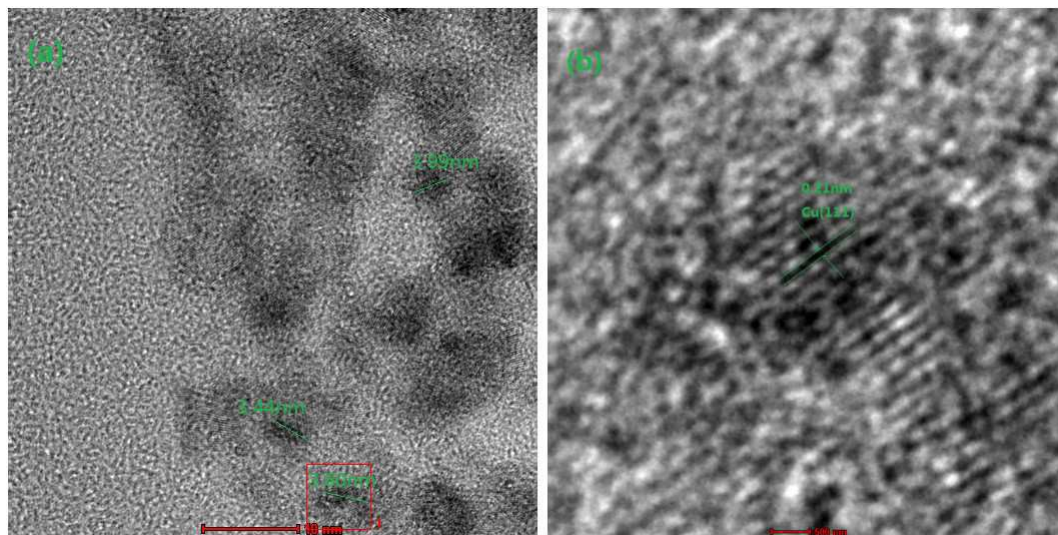
3

for 2h.

4

5

1

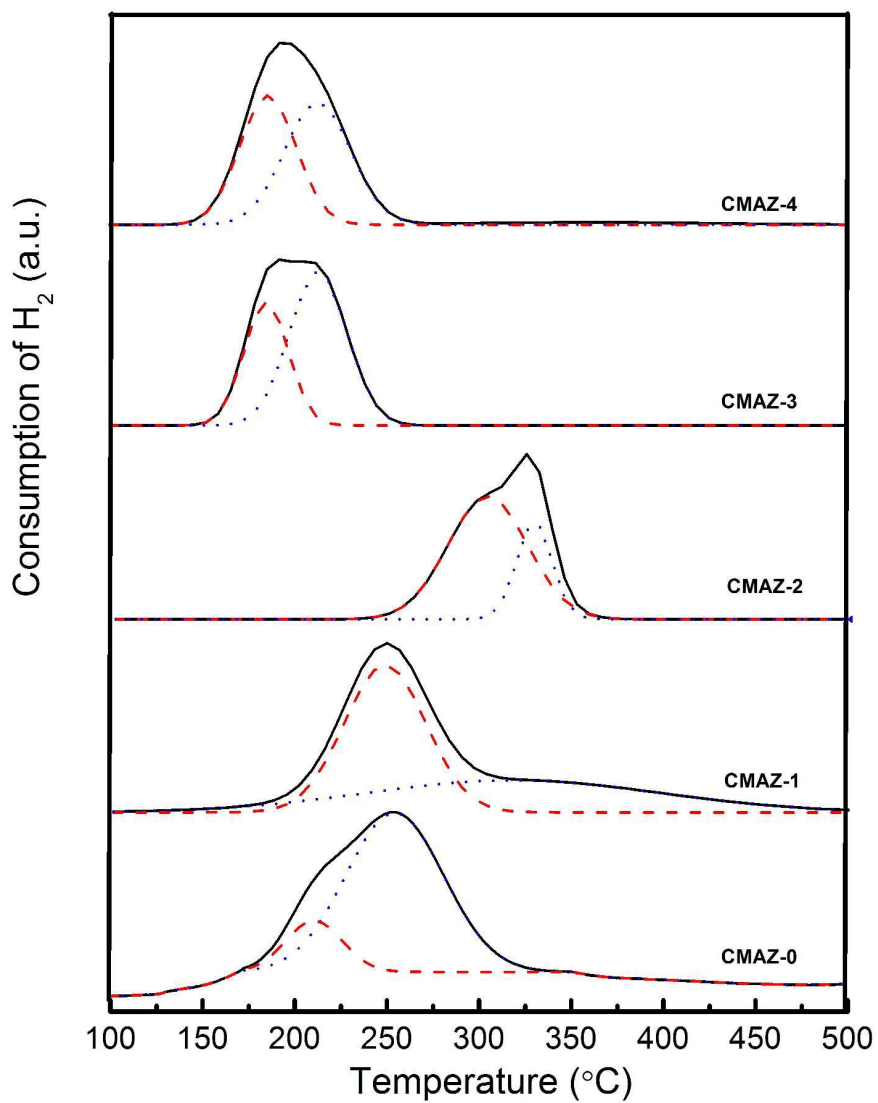


2

**Fig. 5** (a) HRTEM images of CMAZ-1 catalysts after H<sub>2</sub> reduction at 300 °C for 2h.

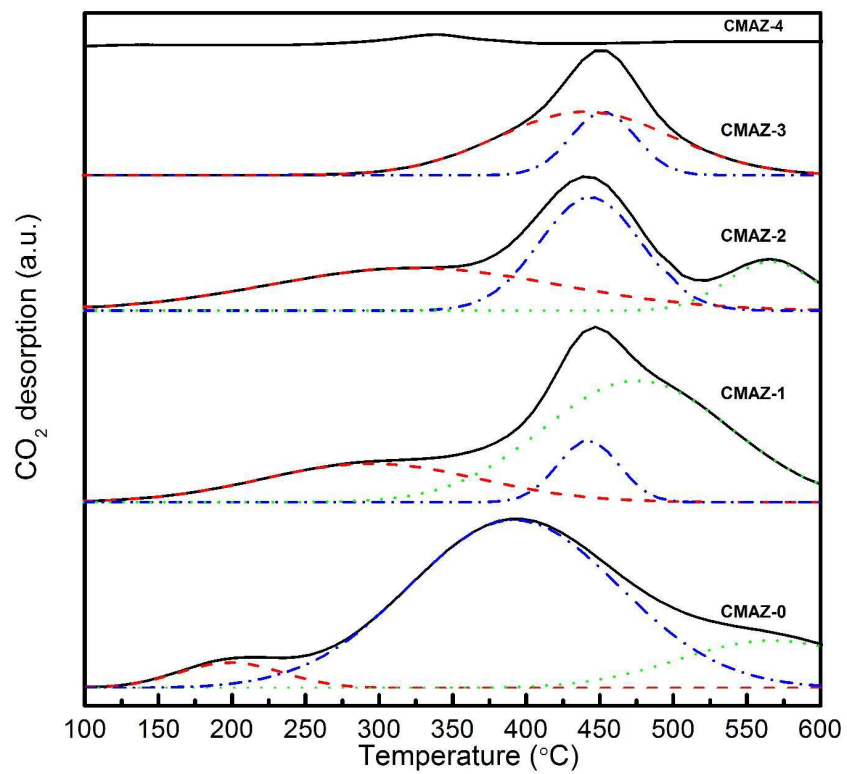
3

(b) HRTEM image of single particle from (a).



1

2 **Fig. 6** H<sub>2</sub>-TPR profiles of catalysts at 450°C, black solid, red dash and blue dot lines  
3 correspond to the TPR,  $\alpha$  and  $\beta$  peak, respectively.



1

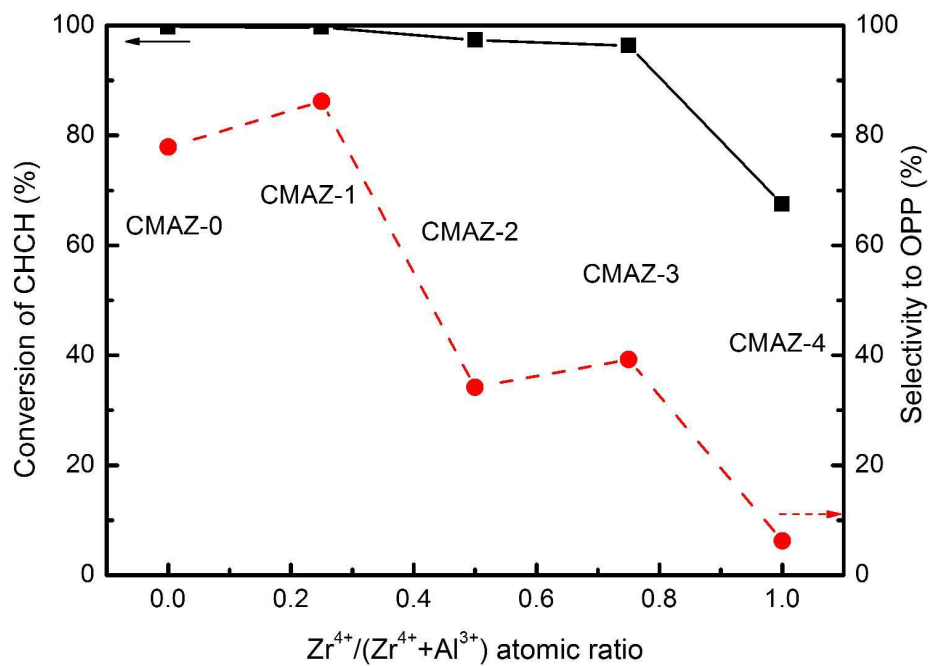
2 **Fig. 7** CO<sub>2</sub>-TPD profiles of the catalysts with various Zr content, black solid, red dash,3 blue dot dash and dot lines correspond to the TPD,  $\alpha$ ,  $\beta$  and  $\gamma$  peak, respectively.

4

5

6

1



2

**Fig. 8** Effects of the amount of Zr on the conversion of OCC and the selectivity

3

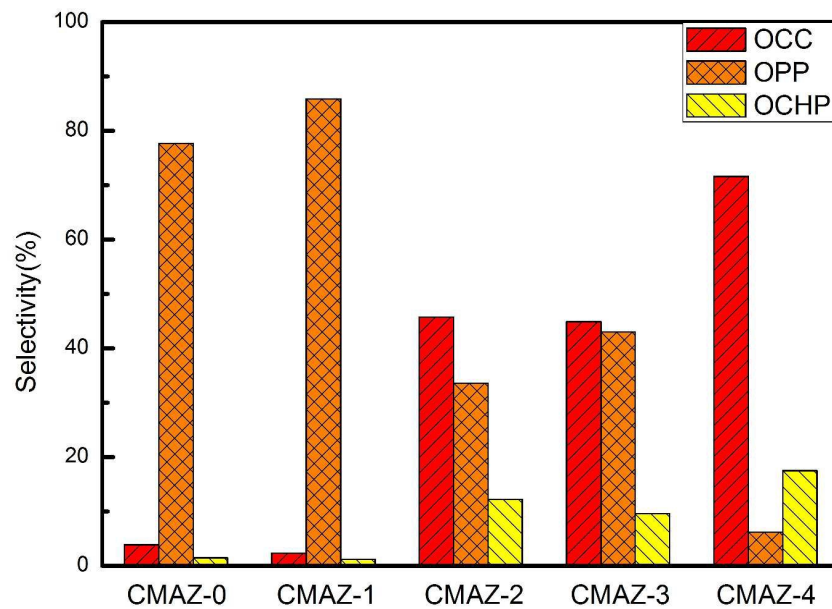
toward OPP at 330 °C after 2 h reaction.

4

5

6

1



2

**Fig. 9** The catalytic selectivity for three primary products of all catalysts after 2 h

3

reaction.

4

5

6

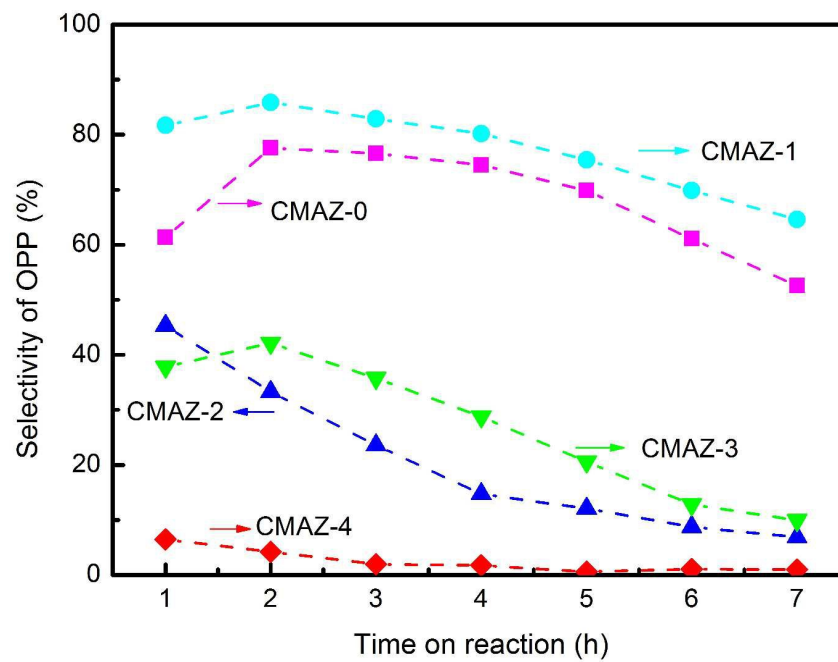


**Fig. 10** The stability for different Zr content catalysts at 330 °C.

1  
2  
3  
4  
5  
6  
7  
8  
9  
10  
11  
12  
13  
14

1

**Table 1** Different samples' FWHM and Cu<sup>0</sup> particles size through XRD patterns.

Sample No.	Cu <sup>2+</sup> /Mg <sup>2+</sup> /Al <sup>3+</sup> /Zr <sup>4+</sup> atomic ratio	FWHM (θ) <sup>a</sup>	d(Cu <sup>0</sup> ) <sub>XRD</sub> (nm)
CMAZ-0	2.5:3.5:2:0	1.545	5.47
CMAZ-1	2.5:3.5:1.5:0.5	2.128	3.97
CMAZ-2	2.5:3.5:1:1	1.271	6.65
CMAZ-3	2.5:3.5:0.5:1.5	0.660	12.81
CMAZ-4	2.5:3.5:0:2	0.639	13.23

2

<sup>a</sup> The FWHM of the Cu<sup>0</sup> particles

3

4

5

6

7

**Table 2** Structural properties of the catalysts with various amount of Zr.

Catalysts	Surface area <sup>a</sup> (m <sup>2</sup> ·g <sup>-1</sup> )	Pore volume <sup>a</sup> (cm <sup>3</sup> ·g <sup>-1</sup> )	Cu surface area <sup>b</sup> (m <sup>2</sup> ·g <sup>-1</sup> )	Cu dispersion <sup>b</sup> (%)
CMAZ-0	133.11	0.358	81.85	12.08
CMAZ-1	134.07	0.789	152.45	22.54
CMAZ-2	97.046	0.340	15.75	2.32
CMAZ-3	35.929	0.128	20.12	2.97
CMAZ-4	66.655	0.409	41.40	6.11

8

<sup>a</sup>After reduction at 300 °C <sup>b</sup>Calculated from dissociative adsorption

**Table 3** Reduction peak temperatures and the percentage of  $\alpha$  peak with different Zr content.

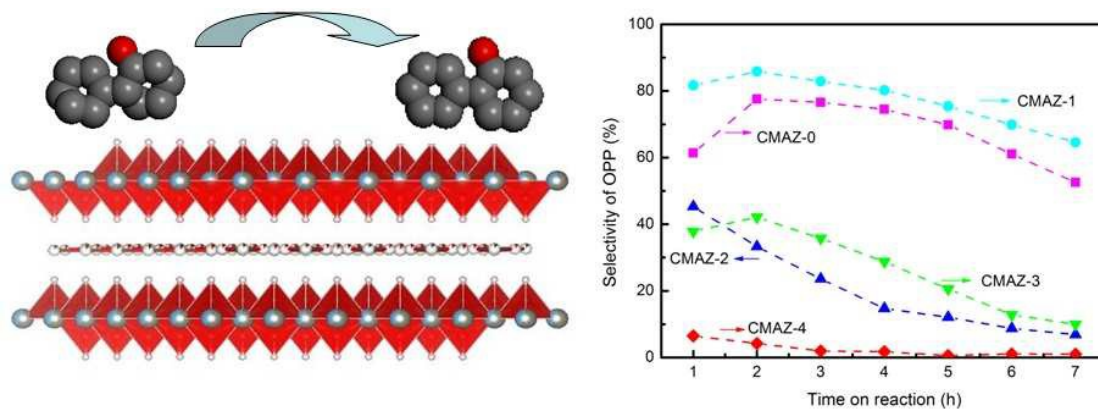
Sample No.	$T_{\alpha}$ (°C)	$T_{\beta}$ (°C)	$A_{\alpha}/(A_{\alpha}+A_{\beta})$ % <sup>a</sup>
CMAZ-0	213	253	14.97
CMAZ-1	249	317	85.32
CMAZ-2	303	330	74.06
CMAZ-3	186	212	38.17
CMAZ-4	186	212	41.38

<sup>a</sup>  $A_{\alpha}$  and  $A_{\beta}$  represent the area of  $\alpha$  and  $\beta$  peaks, respectively.

**Table 4** The basicity and the distribution of basic sites over catalysts with various Zr content.

Sample No.	TPD peak position [temperature (°C)] and concentration (%) <sup>a</sup>		
	Site $\alpha$	Site $\beta$	Site $\gamma$
CMAZ-0	232 (6.01)	446 (79.81)	659 (14.18)
CMAZ-1	295 (23.43)	439 (9.22)	473 (67.35)
CMAZ-2	329 (44.44)	447 (41.89)	566 (13.67)
CMAZ-3	371 (72.73)	385 (27.27)	/
CMAZ-4	/	/	/

<sup>a</sup> The proportion of different basic sites



### Cu/Mg/Al/Zr Non-Noble Metal Catalysts for O-Phenylphenol Synthesis

Yongping Zeng, Tianchi Zhang, Yueyang Xu, Peili Hu, Ting Ye, Zhehua Jia,

Shengui Ju